

UC Davis

UC Davis Previously Published Works

Title

Significant Dzyaloshinskii-Moriya interaction at graphene-ferromagnet interfaces due to the Rashba effect.

Permalink

<https://escholarship.org/uc/item/4k5075n1>

Journal

Nature materials, 17(7)

ISSN

1476-1122

Authors

Yang, Hongxin
Chen, Gong
Cotta, Alexandre AC
[et al.](#)

Publication Date

2018-07-01

DOI

10.1038/s41563-018-0079-4

Peer reviewed

1 **Significant Dzyaloshinskii-Moriya Interaction at Graphene-Ferromagnet**
2 **Interfaces due to Rashba-effect**

3 Hongxin Yang^{1,2,3*,#}, Gong Chen^{4,5*,#}, Alexandre A.C. Cotta^{4,6,7,8}, Alpha T.
4 N'Diaye⁴, Sergey A. Nikolaev¹, Edmar A. Soares⁷, Waldemar A. A. Macedo⁶,
5 Kai Liu⁵, Andreas K. Schmid^{4,#}, Albert Fert² & Mairbek Chshiev^{1,#}

6
7 ¹ Univ. Grenoble Alpes, CEA, CNRS, Grenoble INP, INAC-SPINTEC, 38000 Grenoble,
8 France

9 ² Unité Mixte de Physique, CNRS, Thales, Univ. Paris-Sud, Université Paris-Saclay,
10 Palaiseau 91767, France

11 ³ Key Laboratory of Magnetic Materials and Devices, Ningbo Institute of Materials
12 Technology and Engineering, Chinese Academy of Sciences, Ningbo, Zhejiang 315201,
13 China

14 ⁴ NCEM, Molecular Foundry, Lawrence Berkeley National Laboratory, Berkeley, California
15 94720, USA

16 ⁵ Department of Physics, University of California, Davis, CA, 95616, USA

17 ⁶ Centro do Desenvolvimento da Tecnologia Nuclear, CDTN, 31270-901 Belo Horizonte,
18 MG, Brazil

19 ⁷ Departamento de Física, ICEx, Universidade Federal de Minas Gerais, 31270-901 Belo
20 Horizonte, MG, Brazil

21 ⁸ Present address: Departamento de Física, Universidade Federal de Lavras, 37200-000
22 Lavras, MG, Brazil

23 *These authors contributed equally to the work.

24 # To whom correspondence should be addressed.

25 E-mail: hongxin.yang.spintec@gmail.com, ghenncem@gmail.com, akschmid@lbl.gov,
26 mair.chshiev@cea.fr

27 **The possibility of utilizing the rich spin-dependent properties of graphene has attracted**
28 **great attention in pursuit of spintronics advances. The promise of high-speed and low-**
29 **energy consumption devices motivates a search for layered structures that stabilize**
30 **chiral spin textures such as topologically protected skyrmions. Here we demonstrate**
31 **that chiral spin textures are induced at graphene/ferromagnetic metal interfaces.**
32 **Graphene is a weak spin-orbit coupling material and is generally not expected to induce**
33 **sufficient Dzyaloshinskii-Moriya interaction to affect magnetic chirality. We**
34 **demonstrate that indeed graphene induces a new type of Dzyaloshinskii-Moriya**
35 **interaction due to a Rashba effect. First-principles calculations and experiments using**
36 **spin-polarized electron microscopy show that this graphene-induced Dzyaloshinskii-**
37 **Moriya interaction can have similar magnitude as at interfaces with heavy metals. This**
38 **work paves a path towards two-dimensional material based spin orbitronics.**

39 The unique properties of graphene including well-defined single atomic layer
40 thickness, massless linear dispersion of its electronic structure, and long spin diffusion length
41 have motivated the search for graphene-based phenomena that may enable spintronic
42 applications^{1,2,3}. Recently, graphene was shown to play key roles in several magnetic
43 phenomena, including graphene-based tunnel magnetoresistance^{4,5,6}, enhancement of the
44 spin-injection efficiency^{7,8}, Rashba effect^{9,10}, quantum spin Hall effect¹¹ and large
45 perpendicular magnetic anisotropy (PMA)^{12,13,14}.

46 At the same time, recent progress in the field of spin orbitronics was stimulated by
47 discoveries of phenomena permitting highly efficient electrical control of chiral spin textures,
48 e.g. fast domain wall (DW) dynamics^{15,16,17,18} and skyrmion motion at ultralow current
49 densities^{19,20,21,22}. These findings hold promise for applications in memory^{23,24,25} and logic
50 devices²⁶ where the interfacial Dzyaloshinskii-Moriya Interaction (DMI)^{27,28} has been

51 recognized as a key ingredient in creation, stabilization, and manipulation of
52 skyrmions^{29,30,31,32,33,34} and chiral DWs^{35,36}. While chiral magnetism induced by the
53 interfacial DMI has become an important topic, the DMI at interfaces with graphene was not
54 expected to be significant because, according to the Fert-Levy model³⁷, the DMI scales with
55 spin-orbit coupling (SOC) in the material contacting the ferromagnetic metal (FM) layer³⁸
56 and graphene lacks strong SOC. Recent results reported the observation of enhanced PMA at
57 the graphene/Co interface, even though strong interfacial PMA is also often associated with
58 strong SOC^{14,39}. This suggests that graphene/FM interfaces are unusual: if graphene enhances
59 the PMA at interfaces in the absence of strong SOC, then it is interesting to ask if graphene
60 has similarly strong effects on the DMI helping thereby to promote this and other 2D
61 materials for spin orbitronics. In the following, this idea is tested by exploring the interfaces
62 of graphene with cobalt and nickel, where these two FM elements are chosen for the small
63 lattice mismatch and strong interaction with graphene.

64 **First-principles calculations**

65 The structures of graphene/FM films modelled here are shown in Fig. 1, where a layer
66 of graphene coats the surfaces of three-monolayer (ML) thick hcp Co(0001) and fcc Ni(111)
67 films. Arrows schematically indicate clockwise/right-handed and anticlockwise/left-handed
68 (in parenthesis) spin spiral chirality. The calculated ground state structure is consistent with
69 previous reports^{4,14}, where one carbon atom of the graphene unit cell is located on top of the
70 adjacent Co(Ni) atom and another carbon atom is located above the hollow site, with the
71 graphene/Co(Ni) distance of about 2.12 (2.15) Å.

72 We use the chirality dependent total energy difference approach applied previously
73 for Co/Pt structures^{33,38,40} to calculate microscopic and micromagnetic DMI constants, d^{tot}
74 and D , respectively, as well as the layer-resolved DMI, d^k , where k indicates the individual

75 atomic layers within FM films. As one can see from Fig. 2 for the calculated results, the
 76 largest DMI can reach up to 1.14 meV per atom for a graphene coated single atomic layer of
 77 Co, while for 2 and 3 ML of Co films coated by graphene, the amplitude of d^{tot} drops to 0.16
 78 and 0.49 meV, respectively (Fig. 2a). Moreover, d^{tot} of graphene/Co (brown bars in Fig.2a) is
 79 generally stronger than that of graphene/Ni (green bars in Fig. 2a) for all thicknesses
 80 considered. For the micromagnetic DMI, D , we found that its magnitude decreases as a
 81 function of the FM layer thickness for both graphene coated Co and Ni films, due to
 82 interfacial origin of the DMI leading to the inverse proportionality with respect to FM layer
 83 thickness.³⁸

84 In order to elucidate the origin of such a significant DMI in graphene coated FM, we
 85 then calculated the layer-resolved DMI, d^k , and associated SOC energy difference, ΔE_{SOC}^k , for
 86 the case of graphene coated 3ML Co films. Fig. 2c shows that the largest layer-resolved
 87 DMI, d^k , is located at the interfacial Co layer, labelled as Co1 (blue bar), which is in contact
 88 with graphene, while within the layers further from the interface the DMI decays very fast
 89 (red and black bars), similar to previously reported case at Co/Pt interface³⁸. However,
 90 significant differences between graphene/Co and Co/Pt emerge in terms of where the
 91 corresponding SOC energy source is located. As shown in Fig. 2d, the largest associated
 92 SOC energy difference, ΔE_{SOC}^k , originates from the same Co1 layer rather than from the non-
 93 magnetic side of the interface, where it is almost zero. This is drastically different from the
 94 Co/Pt case where the SOC energy difference is mainly contributed by the adjacent Pt layer.
 95 These findings indicate that the physical mechanism governing the strength of the DMI in
 96 graphene/Co interface is very different from that in Co/Pt, which is captured by the Fert-Levy
 97 model^{37,38}. Instead, in graphene/Co the dominating mechanism is the Rashba-type DMI.
 98 According to the latter^{41,42,43}, the DMI parameter can be roughly expressed as $d = 2k_R A$ at

99 graphene/Co interfaces, where A is the exchange stiffness and $k_R = \frac{2\alpha_R m_e}{\hbar^2}$ is determined by the
 100 Rashba coefficient, α_R , and effective electron mass, m_e . The latter in Co was measured to be
 101 about $0.45 m_0$ ⁴⁴ (with m_0 being the rest mass of electron), and the exchange stiffness, A , was
 102 found to be about 9.5 pJ/m for graphene/Co (3ML)/Ru(0001) based on the Curie temperature
 103 of this structure (see details in Method), which is slightly smaller than $A=15$ pJ/m in thicker
 104 Co films^{34,45}. The Rashba coefficient, α_R , can then be extracted from $\alpha_R=2E_0/k_0$, where E_0 is
 105 the Rashba splitting at the wave vector k_0 . We calculated the Rashba splitting for
 106 graphene/Co(3ML) slab by switching on SOC and putting the magnetization along $\langle 11\bar{2}0 \rangle$
 107 and $\langle \bar{1}\bar{1}20 \rangle$. As one can see in Figs. 2e and f, the corresponding band shifts are a signature of
 108 the Rashba effect even though it deviates slightly from the conventional linear dependence
 109 given by $\alpha_R (\boldsymbol{\sigma} \times \mathbf{k}) \cdot \mathbf{z}$. Different characters of the band splitting at the $\bar{\Gamma}$ point can be attributed
 110 to the fact that Co d orbitals are influenced by different potential gradients due to the
 111 polarization between graphene and Co that provides an intrinsic electric field and
 112 considerably enhances the effective value of SOC at the interface. We chose a band close to
 113 the Fermi level at $\bar{\Gamma}$ point, as shown in Fig. 2f, to estimate the Rashba-type DMI. The Rashba
 114 splitting, E_0 , is about 1.28 meV at $k_0=0.031 \text{ \AA}^{-1}$, and the Rashba coefficient, α_R is thus found
 115 to be about $82.6 \text{ meV} \cdot \text{ \AA}$. This leads to $k_R=9.8 \times 10^{-3} \text{ \AA}^{-1}$ and therefore $d=0.18 \text{ meV}$ at
 116 graphene/Co interfaces, which is smaller than the value calculated from first-principles,
 117 $d=0.49 \text{ meV}$ for graphene coated 3 ML Co films. The reason for the smaller DMI value
 118 extracted from the Rashba effect can be ascribed to the fact that the Rashba-type DMI was
 119 estimated by using only one band close to the Fermi level. As reported in recent studies⁴⁶, the
 120 magnitude and sign of α_R is generally band-dependent due to band-specific orbital orderings
 121 of the orbital angular momentum giving rise to the band-dependent orbital chirality.

122 **Experimental observation of graphene-induced DMI**

123 Experimental tests of the DMI were done using spin-polarized low-energy electron
124 microscopy (SPLEEM), by directly imaging DWs in perpendicularly magnetized films (see
125 Methods). The films were prepared *in-situ* by molecular beam epitaxy under ultrahigh
126 vacuum conditions so that possible extrinsic influences such as growth front roughness are
127 minimal and controlled⁴⁷. The sign of the DMI can be determined by observing the chirality
128 of DWs^{32,36,48}, while the strength of the DMI vector, d , can be quantified by measuring the
129 film thickness dependence of a transition from chiral Néel walls (in thin films, where the
130 interfacial DMI influences DW texture) to achiral Bloch walls (in thicker films, where
131 dipolar forces outweigh the DMI)^{36,48}. We cannot prepare a free standing graphene/Co
132 bilayer where the thickness of Co is several ML, instead, high quality graphene/Co samples
133 were prepared on top of Ru(0001) single-crystal substrates (see Methods).

134 Figs. 3a,b show compound SPLEEM images highlighting the DW spin structure in
135 graphene/Co/Ru(0001) films, where black and grey shades indicate that the magnetization is
136 perpendicular to the film plane with $+M_z$ and $-M_z$ vectors, respectively, while colours
137 represent the in-plane magnetization vector according to the colour wheel (inset). For Co
138 thickness of 3.9 ML (Fig. 3a) the in-plane component of the magnetization within DWs
139 (white arrows) is perpendicular to the DW tangent, and always points from grey domains to
140 black domains, i.e. from $-M_z$ and $+M_z$: this indicates that the DWs have a left-handed/anti-
141 clockwise chiral Néel texture^{36,48}. For Co thickness of 8.4 ML (Fig. 3b), the magnetization
142 vector within DWs is aligned parallel to the DW tangent: this indicates that the DW has a
143 Bloch-type texture. Moreover, the magnetization vector within these DWs reverses its
144 direction in a number of places, indicating that these DWs are achiral Bloch-walls⁴⁹. This
145 thickness-dependent transition of the DW type and chirality can be tracked in more detail

146 using histogram as plotted in Fig. 3c (see Methods). The histogram represents the distribution
147 of the angle α , defined as the angle between the DW magnetization vector \mathbf{m} and the normal
148 direction of DW, \mathbf{n} (Fig. 3c inset). The distribution of the angle α gradually evolves from a
149 single peak around 0° for Co 3.9 ML to double peaks at $\pm 90^\circ$ for Co 8.4 ML thicknesses.

150 The strength of the DMI in this system can be estimated as $d=0.11\pm 0.04$ meV per
151 atom (Fig. 3f), by computing the film thickness related dipolar energy difference between
152 Néel- and Bloch- textured DWs. Note that this analysis is independent of the values of
153 exchange interaction and magnetic anisotropy in a given system (see Methods). The DMI
154 parameter d contains contributions from both the graphene/Co interface and the Co/Ru
155 interface, and the DMI at Co/Ru needs to be tested so that the DMI at graphene/Co can be
156 deduced. In the Co/Ru(0001) system, a spin reorientation transition from out-of-plane to in-
157 plane occurs from 2ML Co to 3ML Co coverage⁵⁰. The step-flow growth mode of this system
158 permits deposition of a Co film of 2.4ML coverage that consists of alternating strips of 2ML
159 and 3ML thickness, featuring out-of-plane- and in-plane domains with well-defined areas
160 (Supplementary Fig. S1). Analogous to Ref. 51, the magnetic structure of this sample is an
161 inhomogeneous spin spiral. SPLEEM imaging (Fig. 3d) and analysis of histograms of the
162 domain wall magnetization angle α indicates that the Co/Ru system features right-handed
163 Néel-type chirality. In detail, the split double peak near $\alpha = 180^\circ$ in the histogram plotted in
164 Fig. 3e indicates DW spin textures point roughly 45° with respect to the domain boundary,
165 where the DMI energy is comparable to the dipolar energy difference between Néel- and
166 Bloch- textured DWs. From this observation the DMI at Co/Ru can be estimated as $d =$
167 -0.05 ± 0.01 meV per atom (see Methods). The DMI is very localized at the interface^{38,40},
168 and in both Co/Ru and graphene/Co/Ru samples the Co layer is either pseudomorphic (hcp,
169 for 1 ML Co thickness) or a moiré structure chiefly composed of alternating fcc and hcp

170 regions (for 2 ML or larger Co thickness, see details in Methods). From the experimental
171 DMI values of Graphene/Co/Ru and Co/Ru, the DMI of the Graphene/Co interface with 4-
172 6ML Co can be determined to be $d = 0.16 \pm 0.05$ meV per atom (Fig. 3f) (see more details
173 in Methods), which is opposite and about three times as strong as the DMI at the Co/Ru
174 interface. This is consistent with the calculated DMI of $d = 0.18$ meV for
175 Graphene/Co[3ML] based on the Rashba model discussed above.

176 **Towards a giant DMI in graphene-based heterostructures**

177 It was previously proposed that the DMI can be amplified using multilayer
178 structures^{34,36,40,52}. As summarized in Fig. 2, the sign of the DMI for graphene/Ni with Ni
179 thickness of 1 and 2 MLs is negative (clockwise/right-handed chirality), while for
180 graphene/Co the sign is always positive (anticlockwise/left-handed chirality). This suggests
181 the possibility to obtain large DMI values by building ternary superlattices based on
182 graphene/Co/Ni heterostructures. We tested this hypothesis with first-principles calculations
183 by modelling graphene/[Co/Ni/graphene]_n structures (Fig. 4). The calculated value of d
184 increases with respect to the number of repeating units, n , with a slope less than one. Further
185 calculations indicate that the amplification of the DMI can be further enhanced in Van der
186 Waals heterostructures where two FM layers are separated by two MLs of graphene, i.e. in
187 multilayers of the graphene/[Co/Ni/bilayer-graphene]_(m-1)/Co/Ni/graphene structure. The
188 result obtained for $m=2$ with $d = 1.13$ meV suggests that in multilayers of n repeating units
189 the DMI approaches a value of m times the DMI of a single graphene/Co/Ni/graphene unit.
190 Furthermore, calculating the PMA for graphene/[Co/Ni/graphene]_n heterostructures shows a
191 linear increase with the number of repeating units n , that is similar to the behaviour of
192 graphene/[Co/graphene]_n reported before¹⁴.

193 From the values of the DMI at Co/graphene interfaces obtained in this work, we

194 predict that graphene induced DMI should be sufficient to stabilize magnetic chiral spin
195 textures in ultrathin FM films attached to graphene. For instance, magnetic chiral DWs and
196 skyrmions have been observed in weak DMI systems (-0.12 meV per atom at Ni/Ir
197 interface⁴⁸, or 0.15 meV per atom in Fe/Ni/Cu system³⁶). The proposed [Co/Ni/graphene]_n
198 heterostructure allows simultaneous enhancement of the DMI and PMA, which may be
199 helpful for stabilizing chiral spin textures such as skyrmions with an extremely small size.
200 Moreover, graphene/Co(Ni) grown on copper could be interesting since graphene production
201 on copper is a well-established process⁵³, where the graphene related interface is expected to
202 dominate the DMI due to the ignorable DMI at Co(Ni)/Cu interface⁵².

203 In summary, we have discovered both from first-principles calculations and from
204 magnetic imaging experiments that graphene/FM interface generates significant DMI. We
205 showed that the physical origin of this DMI is the Rashba-effect. The discovery of the DMI
206 induced by graphene along with its distinctive electronic properties⁵⁴, enhancement of PMA¹⁴,
207 and its ability to act as an excellent capping layer⁵⁵, may open up a new area in the field of
208 spintronics.

209 **ACKNOWLEDGEMENTS**

210 This work was supported by the European Union's Horizon 2020 Research and Innovation
211 Programme under grant agreement No. 696656 (GRAPHENE FLAGSHIP), the ANR
212 ULTRASKY, SOSPIN. *Ab initio* calculations used resource of GENCI-CINES with grant No.
213 C2016097605. Work at the Molecular Foundry was supported by the Office of Science,
214 Office of Basic Energy Sciences, of the U.S. Department of Energy under Contract No. DE-
215 AC02-05CH11231. Work at UCD was supported by the UC Office of the President
216 Multicampus Research Programs and Initiatives MRP-17-454963 (G.C.) and NSF DMR-
217 1610060 (K.L.). A.A.C.C., W.A.A.M. and E.A.S. acknowledge the support of Brazilian

218 agencies CAPES, CNPq and FAPEMIG. H.X.Y. would like also to acknowledge the 1000
219 Talents Program for Young Scientists of China and Ningbo 3315 Program. We thank V.
220 Cros, O. Boule, G. Gaudin, I. M. Miron, T. P. Ma and A. Thiaville for fruitful discussions
221 and comments.

222 **AUTHOR CONTRIBUTIONS**

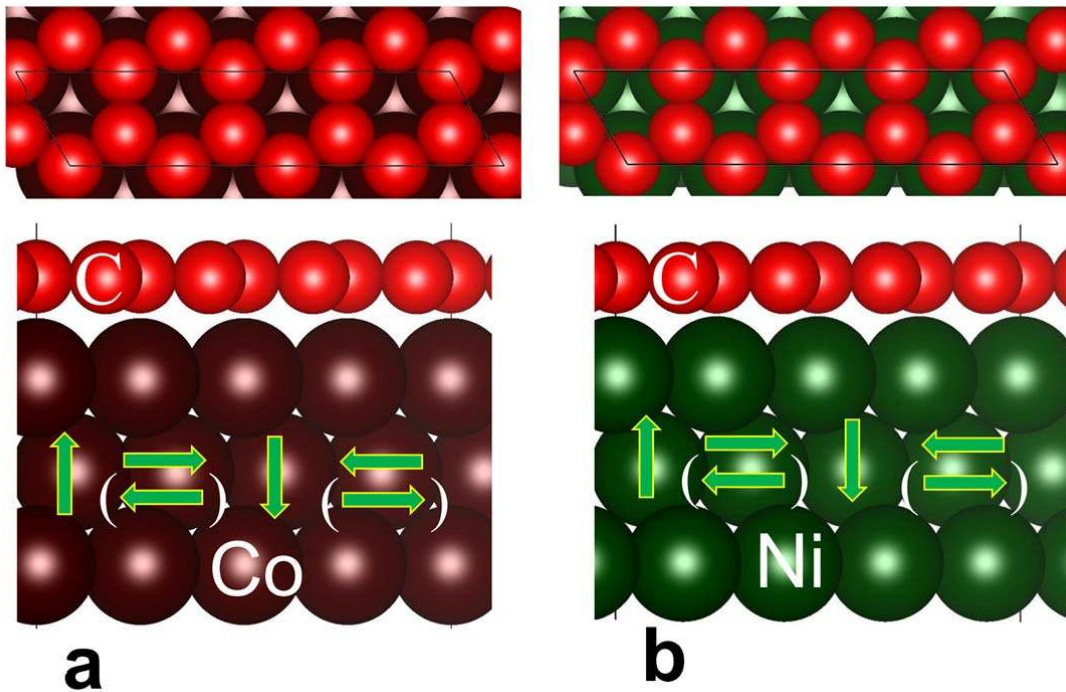
223 H.X.Y. and G.C. conceived the study. H.X.Y and S.A.N. performed the *ab-initio* calculations
224 with help of M.C. H.X.Y., M.C., S.A.N. and A.F. analyzed and interpreted the *ab-initio*
225 results. G.C. and A.A.C.C. carried out the SPLEEM measurements. A.K.S. supervised the
226 SPLEEM facility. G.C., A.A.C.C., A.T.N., K.L., A.K.S analyzed the SPLEEM results. G.C.
227 derived DMI strength from experimental data. G.C., A.A.C.C., A.T.N., K.L., A.K.S., E.A.S,
228 W.A.A.M., interpreted and discussed the experimental result. A.A.C.C., E.A.S, W.A.A.M.
229 performed XPS measurement. H.X.Y and G.C. prepared the manuscript with help from
230 A.A.C.C., A.K.S., S.A.N. and M.C. All authors commented on the manuscript.

231 **COMPETING INTERESTS STATEMENT**

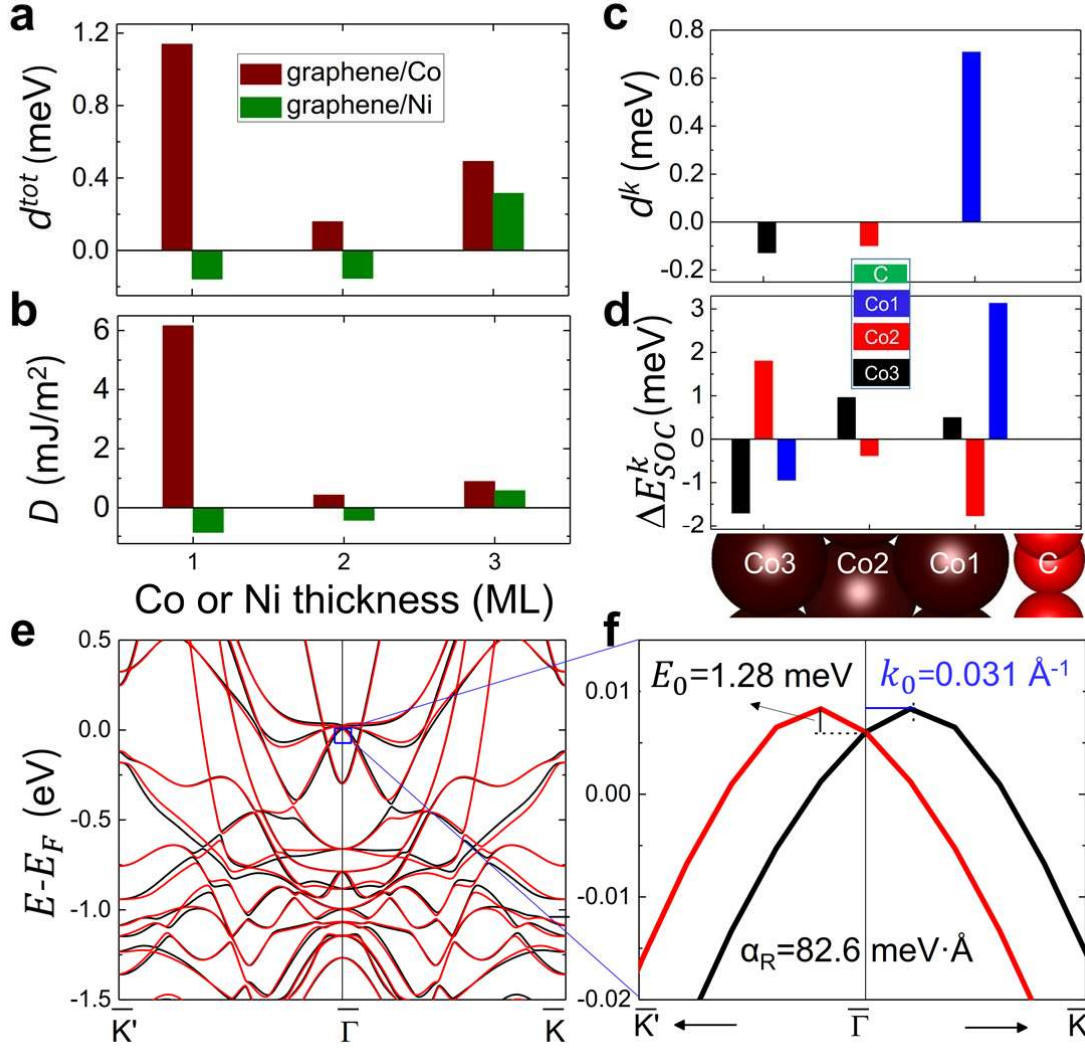
232 The authors declare that they have no competing financial interests.

233

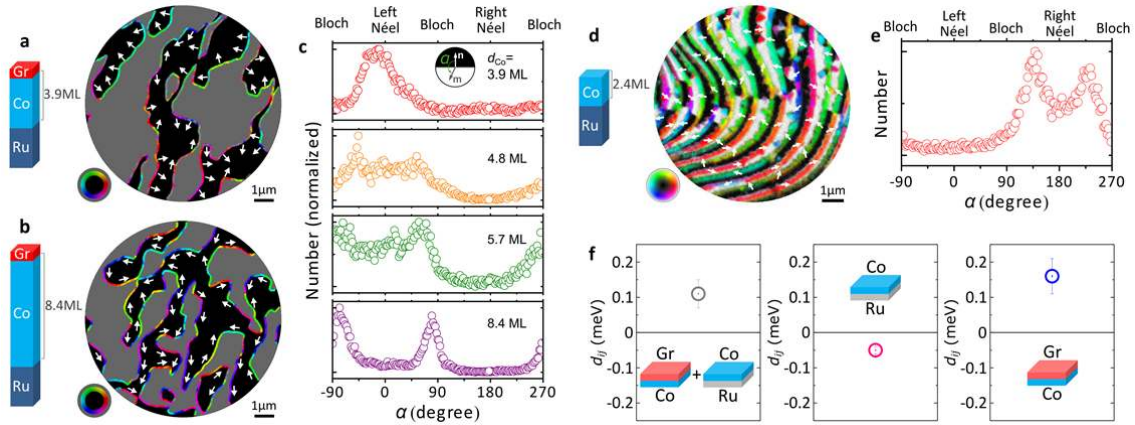
Figure Captions



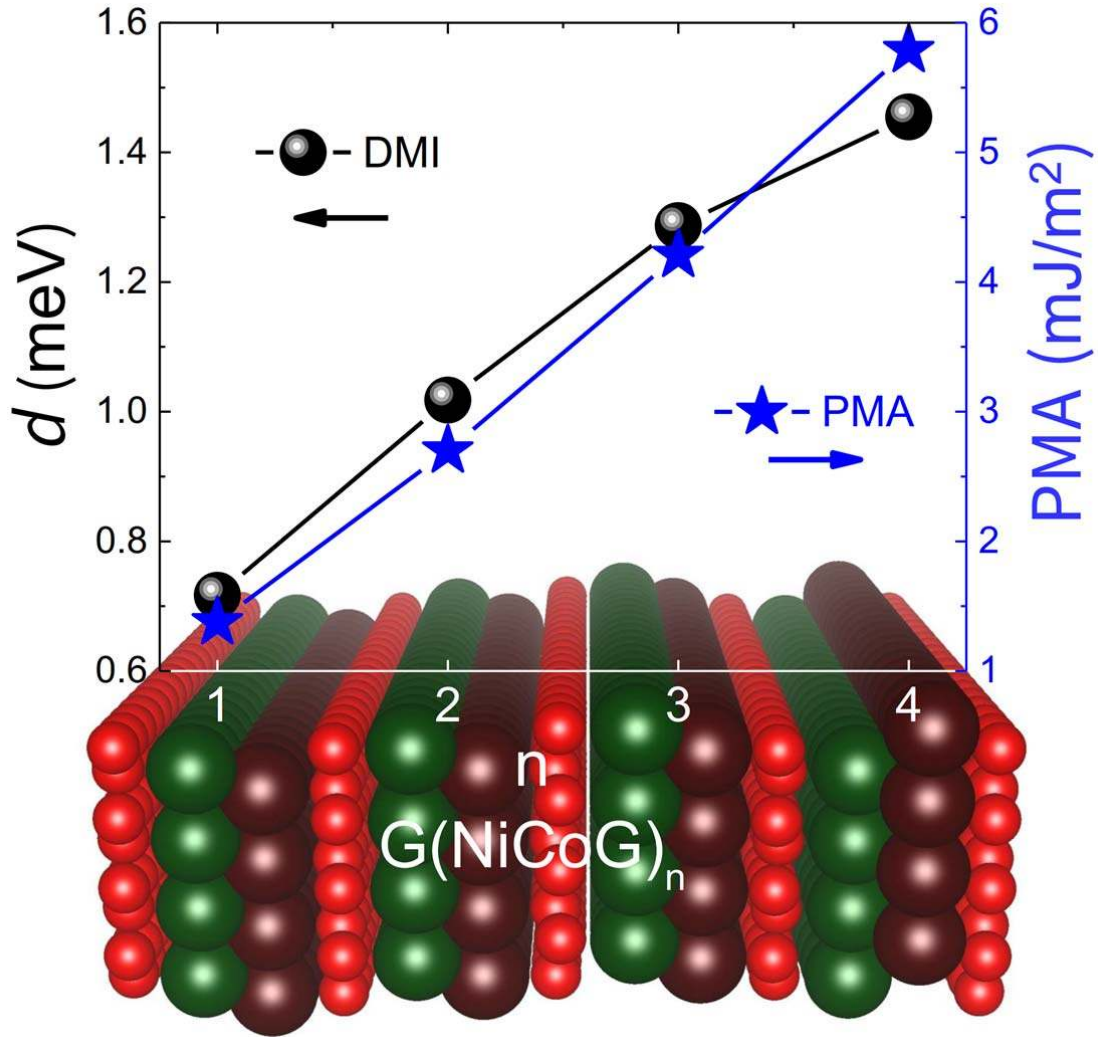
234 **Figure 1** Crystal and spin configurations of graphene coated Co and Ni films used for
235 **DMI calculations.** **a**, Top- and side-view of graphene on hcp Co(0001) and **b**, top- and side-
236 view of graphene on fcc Ni(111) surface. Red, purple and green balls represent carbon, cobalt
237 and nickel atoms, respectively. Clockwise (anticlockwise) spin configurations are
238 schematically shown by arrows.



239 **Figure 2 Anatomy of DMI for graphene/Co and graphene/Ni bilayers.** **a**, Total DMI
 240 coefficient d^{tot} and **b**, micromagnetic DMI coefficient D , as a function of FM film thickness
 241 for graphene/Co (brown bars) and graphene/Ni (green bars) slabs. **c**, Layer-resolved DMI
 242 coefficient d^k of the k^{th} layer for graphene/Co(3ML) slab. **d**, Atomic layer resolved
 243 localization of the associated spin-orbit energy ΔE_{SOC}^k . As it is seen, the large DMI coefficient
 244 of the Co1 layer (blue bar in **c**) is associated with large variations of the SO energy ΔE_{SOC}^{Co1} in
 245 the Co1 layer (see the corresponding blue bar in **d**). **e** and **f**, Band structures for
 246 graphene/Co(3ML) slab with the magnetization axis along $\langle 11\bar{2}0 \rangle$ (black) and $\langle \bar{1}\bar{1}20 \rangle$ (red)
 247 used to estimate the Rashba splitting. The corresponding DMI is found to be about 0.18 meV.



248 **Figure 3** Experimental measurement of DMI in graphene/Co by using SPLEEM. **a,b,**
 249 Compound SPLEEM images of graphene/Co/Ru. Scale bar, $1\mu\text{m}$. White arrows indicate the
 250 orientation of in-plane magnetization. **c,** Co thickness dependent histogram of the angle α
 251 counted pixel-by-pixel at the DW boundary in graphene/Co/Ru(0001) shows the evolution of
 252 the chirality from a left-handed Néel wall (single peak at 0°) to an achiral Bloch wall (double
 253 peaks at $\pm 90^\circ$). Inset shows the definition of the angle α , where \mathbf{m} is the in-plane direction of
 254 the DW magnetization, and \mathbf{n} is the in-plane vector normal to the domain boundary and
 255 always points from grey domains to black domains. **d,** Compound SPLEEM image of Co/Ru.
 256 Scale bar, $1\mu\text{m}$. **e,** the angle α histogram in Co/Ru indicates right-handed Néel-type rotation.
 257 **f,** Calculated DMI vector d_{ij} strength.



259 **Figure 4 DMI and PMA for the multilayer of graphene/[Co/Ni/graphene]_n as a function**
 260 **of the junction number n .** Black points pointing to the left scale and blue stars pointing to
 261 the right scale represent the calculated DMI and PMA values, respectively. Both the DMI and
 262 PMA increase approximately linearly as a function of the junction number n . The atoms
 263 represented by different colours are the same as in Figure 1.
 264

-
- ¹ Castro Neto, A. H., Guinea, F., Peres, N. M. R., Novoselov, K. S. & Geim, A. K. The electronic properties of graphene. *Rev. Mod. Phys.* **81**, 109–162 (2009).
- ² Han, W., Kawakami, R. K., Gmitra, M. & Fabian, J. Graphene spintronics. *Nat. Nanotech.* **9**, 794–807 (2014).
- ³ Roche, S. et al. Graphene spintronics: the European Flagship perspective. *2D Materials* **2**, 030202 (2015).
- ⁴ Karpan, V. M. et al. Graphite and Graphene as Perfect Spin Filters. *Phys. Rev. Lett.* **99**, 176602 (2007).
- ⁵ Cobas, E., Friedman, A. L., van't Erve, O. M. J., Robinson, J. T. & Jonker, B. T. Graphene As a Tunnel Barrier: Graphene-Based Magnetic Tunnel Junctions. *Nano Lett.* **12**, 3000–3004 (2012).
- ⁶ Bodepudi, S. C., Singh, A. P. & Pramanik, S. Giant Current-Perpendicular-to-Plane Magnetoresistance in Multilayer Graphene as Grown on Nickel. *Nano Lett.* **14**, 2233 (2014).
- ⁷ Han, W. et al. Tunneling spin injection into single layer graphene. *Phys. Rev. Lett.* **105**, 167202 (2010).
- ⁸ Dlubak, B. et al. Highly efficient spin transport in epitaxial graphene on SiC. *Nat. Phys.* **8**, 557–561 (2012).
- ⁹ Dedkov, Yu. S., Fonin, M., Rüdiger, U. & Laubschat, C. Rashba Effect in the Graphene/Ni(111) System. *Phys. Rev. Lett.* **100**, 107602 (2008).
- ¹⁰ Liu, M.-H., Bundesmann, J. & Richter, K. Spin-dependent Klein tunneling in graphene: Role of Rashba spin-orbit coupling. *Phys. Rev. B* **85**, 085406 (2012).
- ¹¹ Kane, C. L. & Mele, E. J. Quantum spin Hall effect in graphene. *Phys. Rev. Lett.* **95**, 226801 (2005).
- ¹² Vo-Van, C. et al. Ultrathin epitaxial cobalt films on graphene for spintronic investigations and applications, *New J. Phys.* **12**, 103040 (2010)
- ¹³ Rougemaille, N. et al. Perpendicular magnetic anisotropy of cobalt films intercalated under graphene, *Appl. Phys. Lett.* **101**, 142403 (2012)
- ¹⁴ Yang, H. X. et al. Anatomy and Giant Enhancement of the Perpendicular Magnetic Anisotropy of Cobalt-Graphene Heterostructures. *Nano Lett.* **16**, 145 (2015).
- ¹⁵ Miron, I. M. et al. Fast current-induced domain-wall motion controlled by the Rashba effect. *Nat. Mater.* **10**, 419–423 (2011).
- ¹⁶ Emori, S., Bauer, U., Ahn, S.-M., Martinez, E. & Beach, S. D. Current-driven dynamics of chiral ferromagnetic domain walls. *Nat. Mater.* **12**, 611 (2013).
- ¹⁷ Ryu, K.-S., Thomas, L. Yang, S.-H. & Parkin, S. Chiral spin torque at magnetic domain walls. *Nat. Nanotech.* **8**, 527 (2013).
- ¹⁸ Haazen, P. P. J. et al. Domain wall depinning governed by the spin Hall effect. *Nat. Mater.* **12**, 299 (2013).
- ¹⁹ Jonietz F. et al. Spin Transfer Torques in MnSi at Ultralow Current Densities. *Science* **330**, 1648-1651 (2010)
- ²⁰ Romming, N. et al., Writing and Deleting Single Magnetic Skyrmions. *Science* **341**, 634 (2013).
- ²¹ Yu, X.Z. et al., Skyrmion flow near room temperature in an ultralow current density. *Nat. Communications* **3**, 988 (2012).
- ²² Iwasaki, J., Mochizuki, M. & Nagaosa, N. Current-induced skyrmions in constricted geometries. *Nat. Nanotech.* **8**, 742 (2013).

-
- ²³ Parkin, S. S. P., Hayasi, M. & Thomas, L. Magnetic Domain-Wall Racetrack Memory. *Science* **320**, 197202 (2009).
- ²⁴ Fert, A., Cros, V. & Sampaio, J. Skyrmions on the track. *Nat. Nanotech.* **8**, 152–156 (2013).
- ²⁵ Nagaosa, N. & Tokura, Y. Topological properties and dynamics of magnetic skyrmions. *Nat. Nanotech.* **8**, 899–911 (2013).
- ²⁶ Allwood, D. A., et al. Magnetic domain-wall logic. *Science* **309**, 1688-1692 (2005).
- ²⁷ Dzyaloshinskii, I. E. *Sov. Phys. JETP* **5**, 1259 (1957).
- ²⁸ Moriya, T. Anisotropic superexchange interaction and weak Ferromagnetism. *Phys. Rev.* **120**, 91–98 (1960).
- ²⁹ Yu, X. Z. et al. Real-space observation of a two-dimensional skyrmion crystal. *Nature* **465**, 901–904 (2010).
- ³⁰ Sampaio, J., Cros, V., Rohart, S., Thiaville, A. & Fert, A. Nucleation, stability and current-induced motion of isolated magnetic skyrmions in nanostructures. *Nat. Nanotech.* **8**, 839–844 (2013).
- ³¹ Jiang, W. et al. Blowing magnetic skyrmion bubbles. *Science* **349**, 283 (2015).
- ³² Chen, G. et al. Room temperature skyrmion ground state stabilized through interlayer exchange coupling. *Appl. Phys. Lett.* **106**, 242404 (2015).
- ³³ Boulle, O. et al. Room-temperature chiral magnetic skyrmions in ultrathin magnetic nanostructure. *Nat. Nanotech.* **11**, 449 (2016).
- ³⁴ Moreau-Luchaire, C. et al. Additive interfacial chiral interaction in multilayers for stabilization of small individual skyrmions at room temperature. *Nat. Nanotech.* **11**, 444 (2016).
- ³⁵ Thiaville, A., Rohart, S., Jué, É., Cros, V. & Fert, A. Dynamics of Dzyaloshinskii domain walls in ultrathin magnetic films. *Europhys. Lett.* **100**, 57002 (2012).
- ³⁶ Chen, G. et al. Novel Chiral Magnetic Domain Wall Structure in Fe/Ni/Cu(001) Films. *Phys. Rev. Lett.* **110**, 177204 (2013).
- ³⁷ Fert, A. & Levy, P. M. Role of Anisotropic Exchange Interactions in Determining the Properties of Spin-Glasses. *Phys. Rev. Lett.* **44**, 1538–1541 (1980)
- ³⁸ Yang, H., Thiaville, A., Rohart, S., Fert, A. & Chshiev, M. Anatomy of Dzyaloshinskii–Moriya interaction at Co/Pt interfaces. *Phys. Rev. Lett.* **115**, 267210 (2015).
- ³⁹ Dieny, B. & Chshiev, M. Perpendicular magnetic anisotropy at transition metal/oxide interfaces and applications, *Rev. Mod. Phys.* **89**, 025008 (2017).
- ⁴⁰ Yang, H. X., Boulle, O., Cros, V., Fert, A. & Chshiev, M. Controlling Dzyaloshinskii–Moriya Interaction via Chirality Dependent Layer Stacking, Insulator Capping and Electric Field. *arXiv:1603.01847* (2016).
- ⁴¹ Kundu, A. and Zhang, S. Dzyaloshinskii–Moriya interaction mediated by spin-polarized band with Rashba spin-orbit coupling. *Phys. Rev. B* **92**, 094434 (2015).
- ⁴² Imamura, H., Bruno, P. and Utsumi, Y. Twisted exchange interaction between localized spins embedded in a one- or two-dimensional electron gas with Rashba spin-orbit coupling. *Phys. Rev. B* **69**, 121303(R) (2015).
- ⁴³ Kim, K.-W., Lee, H.-W., Lee, K.-J. & Stiles, M. D. Chirality from interfacial spin-orbit coupling effects in magnetic bilayers. *Phys. Rev. Lett.* **111**, 216601 (2013).
- ⁴⁴ Bode, S., Starke, K. & Kaindl, G. Spin-dependent surface band structure of hcp Co(10 $\bar{1}$ 0). *Phys. Rev. B* **60**, 2946 (1999).

-
- ⁴⁵ Eyrieh, C. et al. Effects of substitution on the exchange stiffness and magnetization of Co films. *Phys. Rev. B* **90**, 235408 (2014).
- ⁴⁶ Park, J.-H. et al. Orbital chirality and Rashba interaction in magnetic bands. *Phys. Rev. B* **87**, 041301(R) (2013).
- ⁴⁷ Lee-Hone, N. R., et al. Roughness-induced domain structure in perpendicular Co/Ni multilayers. arXiv:1612.04867 (2016).
- ⁴⁸ Chen, G. et al. Tailoring the chirality of magnetic domain walls by interface engineering. *Nat. Commun.* **4**, 2671 (2013).
- ⁴⁹ Chen, G. et al. Unlocking Bloch-type chirality in ultrathin magnets through uniaxial strain. *Nat. Commun.* **6**, 6598 (2015).
- ⁵⁰ El Gabaly, F. et al. Imaging spin-reorientation transitions in consecutive atomic Co layers on Ru (0001). *Phys. Rev. Lett.* **96** (14), 147202 (2006)
- ⁵¹ Meckler, S. et al. Real-space observation of a right-rotating inhomogeneous cycloidal spin spiral by spin-polarized scanning tunneling microscopy in a triple axes vector magnet. *Phys. Rev. Lett.* **103**, 157201 (2009).
- ⁵² Chen, G. et al. Ternary superlattice boosting interface-stabilized magnetic chirality. *Appl. Phys. Lett.* **106**, 062402 (2015).
- ⁵³ Li, X. et al. Large-Area Synthesis of High-Quality and Uniform Graphene Films on Copper Foils. *Science* **324**, 1312-1314 (2009).
- ⁵⁴ Geim, A. K. & Novoselov, K. S. The rise of graphene. *Nat. Mater.* **6**, 183 - 191 (2007).
- ⁵⁵ Coraux, J. et al. Air-protected epitaxial graphene/ferromagnet hybrids prepared by chemical vapor deposition and intercalation. *J. Phys. Chem. Lett.* **3**, 2059-2063 (2012).

265 **METHODS**

266 **First-principles calculations.** The Vienna *ab initio* simulation package (VASP) was used in
267 our calculations with electron-core interactions described by the projector augmented wave
268 method, and the exchange correlation energy calculated within the generalized gradient
269 approximation of the Perdew-Burke-Ernzerhof (PBE) form^{56,57}. The cutoff energies for the
270 plane wave basis set used to expand the Kohn-Sham orbitals were chosen to be 520 eV for all
271 calculations. The Monkhorst-Pack scheme was used for the Γ -centred $4\times 16\times 1$ k -point mesh.
272 In order to extract the DMI vectors, the calculations were performed in three steps. First, the
273 corresponding structures were relaxed until the forces become smaller than 0.001 eV/Å to
274 determine the most stable interfacial geometries. In our DMI calculations, we coated 1 to 3
275 monolayers of hcp Co(0001) or fcc Ni(001) films by graphene in a 4 by 1 surface unit cell
276 with $\pi/2$ spin rotations (Fig. 1), we also calculated hcp- or fcc stacked Co films on bare
277 Ru(0001) in same unit cell. Next, the Kohn-Sham equations were solved with no spin-orbit
278 interaction taken into account to find out the charge distribution of the system's ground state.
279 Finally, spin-orbit coupling was included and the self-consistent total energy of the systems
280 was determined as a function of the constrained magnetic moments. We employ the same
281 method used for DMI calculations in frustrated bulk systems and insulating chiral-lattice
282 magnets⁵⁸ and adapted to the case of interfaces. As for the Rashba effect, we adopted the
283 same approach as in Ref. [59] (see also Supplementary Fig. S.2 and corresponding
284 discussion).

285 **Sample preparation.** We conducted the experiments in the SPLEEM system at National
286 Center for Electron Microscopy of Lawrence Berkeley National Laboratory. All samples
287 were prepared under ultra-high vacuum (UHV) conditions, with base pressure better than
288 4.0×10^{-11} Torr. Ru(0001) substrates were cleaned by repeated flash annealing at 1470 K in

289 3.0×10^{-8} Torr O^2 atmosphere and final annealing at 1430 K under UHV. After such
290 procedure, we did not observe any trace of contaminants by Auger electron spectroscopy
291 (AES) and LEEM. Furthermore, high-quality low energy electron diffraction patterns were
292 obtained, indicating a well-ordered surface.

293 Graphene was grown by chemical vapour deposition method⁵⁵, where we kept the
294 substrate at 920 K under ethylene atmosphere (10^{-8} Torr) for around 15 minutes, while
295 observing the process by LEEM. Preparing graphene at low growth temperature is required
296 for a good intercalation process, since defects within the graphene layer assist the cobalt
297 migration. The presence of graphene was confirmed by the moiré pattern in low energy
298 electron diffraction⁶⁰ (see Supplementary Fig. S.3). After cooling graphene/Ru(0001) to
299 room temperature, an amount of one monolayer Co was deposited by electron beam
300 evaporation at rates of 0.18 ML per minute, and intercalated by annealing at 620 K for 3
301 minutes⁶¹. In order to achieve higher Co thicknesses, we repeated the intercalation of
302 additional monolayer-doses of Co, exploring layer thicknesses up to 24 ML Co. The Co
303 growth rate was calibrated by monitoring the LEEM image intensity during the deposition of
304 Co directly onto bare Ru (0001). For the Co/Ru films, Co layers were deposited on Ru(0001)
305 by electron beam evaporation at 460 K substrate temperature, promoting step flow growth
306 mode. The atomic layer thickness of the Co deposit is known directly from monitoring the
307 step flow growth in-situ in LEEM.

308 The growth of magnetic layers was monitored by low-energy electron diffraction
309 (LEED). All of the samples show sharp diffraction patterns, indicating well-defined
310 crystallinity and epitaxy (see Supplementary Fig. S.4). The 1st Co layer grows
311 pseudomorphic on clean Ru, consistent with Ref. 62. In the presence of graphene, the
312 pseudomorphic structure of one monolayer Co between graphene and Ru(0001) has been

313 reported by scanning tunneling microscopy in Ref. 61 and Ref. 63, where the structure of the
314 graphene moiré pattern remains identical before and after the intercalation of the first
315 monolayer Co, proving that the Co monolayer under the graphene is pseudomorphic with the
316 Ru(0001). For thicker Co coverages, superstructures near the first-order LEED spots (see
317 example in Supplementary Fig. S.4e) have been attributed to relaxation of the lattice
318 mismatch between Co and Ru, resulting in an epitaxial relationship that features Co layers
319 with essentially bulk structure, where lattice mismatch strain is relieved at the Co/Ru
320 interface in a moiré structure composed of alternating hcp and fcc stacked regions⁶².

321 In the graphene/Co/Ru(0001) system increasing the Co film thickness weakens
322 perpendicular magnetic anisotropy, analogous to the findings reported in Ref. 12. This allows
323 us to tailor the effective magnetic anisotropy of our samples by approaching the spin
324 reorientation transition point from out-of-plane to in-plane, where the effective anisotropy
325 can become extremely small. Proximity to the spin reorientation transition results in rather
326 large width of the domain walls⁶⁴, which is useful for the precise mapping of domain wall
327 spin textures in the SPLEEM.

328 Possible signs of Co diffusion into Ru were monitored by X ray photoelectron
329 spectroscopy (XPS) in Co/Ru (0001) films grown by the same procedure as described above.
330 We conducted the XPS experiment at Centro do Desenvolvimento da Tecnologia Nuclear.
331 The measurements were carried out in an ultrahigh vacuum chamber (base pressure better
332 than 2.0×10^{-10} mbar) using an Al K α x-ray source with the output power set at 300 W and a
333 VG Microtech hemispherical electron energy analyzer CLAM 2/1 VU. Normal emission
334 scans with 50 eV pass energy were acquired. Following the Co and Ru XPS signal before and
335 after the annealing procedure, we did not observe any evidence of Co-Ru interdiffusion (see
336 Supplementary Fig. S.5).

337 **Real-space imaging.** In the SPLEEM system, real-space images were acquired using three
338 orthogonal electron beam spin-alignments such that magnetic contrast along three orthogonal
339 directions corresponds to the out-of-plane magnetization direction and two orthogonal in-
340 plane axes⁶⁵, as shown in Supplementary Fig. S.1a-c. SPLEEM images map magnetization of
341 the sample in the sense that intensity in each pixel represents the dot product of the spin
342 polarization vector \mathbf{P} of the illumination beam and the magnetization vector \mathbf{M} . The lateral
343 spatial resolution of the SPLEEM at Berkeley lab is ~ 15 nm, while the measured DW width
344 in the systems studied here is between 150 nm to 350 nm. The energy of the incident electron
345 beam was set to 3.6 eV for graphene/Co/Ru and 5 eV for Co/Ru; these values were chosen to
346 optimize the magnetic contrast. All images were obtained with samples at room temperature.
347 The images are represented in grey scale, where a black and white contrast correspond to the
348 magnetization vector pointing into the film plane ($+M_z$) and out of the plane ($-M_z$),
349 respectively, as shown in Supplementary Fig. S.1a, 1b and 1c. To highlight DW spin
350 structures, the triplets of SPLEEM images representing out-of-plane and orthogonal in-plane
351 magnetization components are combined into single compound images, as shown in
352 Supplementary Fig. S.1e. In this projection, colours represent the in-plane magnetization as
353 indicated by the colour wheel (inset), black and grey values represent the perpendicular
354 magnetization component, $+M_z$ and $-M_z$, respectively.

355 **Analysis of chirality.** The method to analyse DW chirality from the SPLEEM images is the
356 same as described by G. Chen, et al.⁴⁸ First, along all DWs the DW normal direction \mathbf{n} is
357 determined from the out-of-plane magnetization SPLEEM images, where \mathbf{n} is defined as a
358 vector pointing from spin-down ($-M_z$) to spin-up ($+M_z$) domains. Then, at all pixels along the
359 DW centrelines, the in-plane magnetization direction, (\mathbf{m}), is measured from the grey values
360 of the two in-plane SPLEEM images. To improve the signal-noisy ratio, in this step each

361 pixel is averaged with its three nearest neighbour pixels. Finally, we compute the angle α ,
 362 defined as the angle between \mathbf{m} and \mathbf{n} (inset of Fig. 3c), and we calculate its distribution
 363 along all DW centrelines, as represented by the histograms.

364 **Estimating the exchange stiffness.** The strength of the Rashba-induced DMI at graphene/Co
 365 interfaces depends on the value of the exchange stiffness, which, in very thin films, can be
 366 lower than the Co bulk value of 15 pJ/m.³⁴ The exchange stiffness in graphene/Co/Ru(0001)
 367 samples can be estimated from the Curie temperature, which is obtained by real-time
 368 SPLEEM measurement of the temperature dependent magnetization. The Curie temperature

369 T_C depends on the exchange stiffness A as $T_C = \frac{2z_{NN}(g_J-1)^2 J_{ex}}{3k_B} J(J+1)$ where $A = 2 \frac{J_{ex} S^2 z_{NC}}{a}$

370 ⁶⁶, z_{NN} is the number of nearest neighbor atoms, g_J is the g-factor, k_B is the Boltzmann
 371 constant, J is the total angular momentum quantum number, S is the spin quantum number,
 372 z_{NC} is the number of atoms in a unit cell, and a is the lattice constant. For
 373 graphene/Co(3ML)/Ru(0001) we find that the Curie temperature is about 861K (see
 374 Supplementary Fig. S.6). In this sample structure $z_{NN} = 12$, $g_J = 2.09$, $k_B = 1.38 \times$
 375 $10^{-23} \text{ m}^2 \text{ kg s}^{-2} \text{ K}^{-1}$, $J = 1/2$, $S = 1/2$, $z_{NC} = 4$, so the result $T_C^{3ML Co} = 861\text{K}$ leads to
 376 the experimental estimate of A as 9.5 pJ/m for 3ML Co. Measuring thicker films we find that
 377 for graphene/Co(4 ML)/Ru the magnetic contrast remains strong up to above 943K, but in
 378 this temperature range the films are not stable. Thus a lower limit of A in graphene/Co(4
 379 ML)/Ru can be estimated as 10.4 pJ/m and an upper limit of the exchange stiffness in films
 380 of any thickness is the value of bulk Co, 15 pJ/m.

381 **Estimating the DMI strength.** The orientation of magnetization within the domain wall with
 382 respect to the domain boundary direction in Fig. 3 allows one to estimate the strength of the
 383 interfacial DMI, using methods described in more detail in refs. 36 and 48. Briefly, the free

384 energies of Néel and Bloch walls can be written as $E^{\text{Néel}} = E_{\text{EX}}^{\text{Néel}} + E_{\text{A}}^{\text{Néel}} + E_{\text{d}}^{\text{Néel}} + E_{\text{DM}}^{\text{Néel}}$
 385 and $E^{\text{Bloch}} = E_{\text{EX}}^{\text{Bloch}} + E_{\text{A}}^{\text{Bloch}} + E_{\text{d}}^{\text{Bloch}} + E_{\text{DM}}^{\text{Bloch}}$ respectively, where E_{EX} , E_{A} , E_{d} and E_{DM}
 386 correspond to exchange energy, magnetic anisotropy energy, dipolar energy and DMI energy
 387 of the walls, respectively. Néel wall is favoured when $E^{\text{Néel}} < E^{\text{Bloch}}$; and since both the
 388 exchange and magnetic anisotropy energy are degenerate for Néel- and Bloch-type walls and
 389 the interfacial DMI energy vanishes for Bloch-type walls⁴⁹, this inequality can be expressed
 390 as $E_{\text{d}}^{\text{Néel}} + E_{\text{DM}}^{\text{Néel}} < E_{\text{d}}^{\text{Bloch}}$. Likewise, Bloch wall is favoured when $E_{\text{d}}^{\text{Néel}} + E_{\text{DM}}^{\text{Néel}} > E_{\text{d}}^{\text{Bloch}}$.
 391 Thus, from observations of thickness-dependent transitions from Néel to Bloch wall, the
 392 range of $E_{\text{DM}}^{\text{Néel}}$ can be bracketed by computing the dipolar energy contributions. Samples with
 393 thickness below the wall-type transition feature Bloch walls and $E_{\text{d}}^{\text{Bloch}} - E_{\text{d}}^{\text{Néel}} < E_{\text{DM}}^{\text{Néel}}$,
 394 whereas in samples with thickness above the transition walls have Néel structure and
 395 $E_{\text{DM}}^{\text{Néel}} < E_{\text{d}}^{\text{Bloch}} - E_{\text{d}}^{\text{Néel}}$. Using the method for calculating the dipolar energy difference as
 396 described in refs. 36 and 48, the dipolar energy constant D_{dip} is $\frac{\mu_0(d_{\text{Co}}\mu_{\text{Co}})^2}{8\pi a_{\parallel}^3}$ ⁴⁸, where $\mu_0 =$
 397 $4\pi \times 10^{-7} \text{H} \cdot \text{m}^{-1}$, $\mu_{\text{B}} = 9.27 \times 10^{-24} \text{A} \cdot \text{m}^2$, $\mu_{\text{Co}} = 1.7\mu_{\text{B}}$, $a_{\parallel} = 2.51\text{Å}$. Using the Matlab
 398 software, we numerically calculate the dipolar energy difference $E_{\text{d}}^{\text{Bloch}} - E_{\text{d}}^{\text{Néel}}$ of
 399 graphene/Co/Ru(0001) with various thicknesses. In graphene/Co/Ru(0001) films,
 400 observations of Néel walls for Co=3.9ML, tilted walls for Co=4.8ML, and Bloch-like walls
 401 for Co=5.7ML lead to values of $E_{\text{d}}^{\text{Bloch}} - E_{\text{d}}^{\text{Néel}} = -0.38 \text{ meV per atom}$,
 402 $-0.58 \text{ meV per atom}$ and $-0.81 \text{ meV per atom}$, respectively. Note that the dipolar energy
 403 cost of Néel walls $E_{\text{d}}^{\text{Néel}}$ is greater than that of Bloch walls $E_{\text{d}}^{\text{Bloch}}$ [36,48], therefore all
 404 numbers calculated above are negative. In the calculation, the width of domain walls is
 405 chosen as 150nm, which is consistent with estimates of both Néel and Bloch walls observed
 406 in the SPLEEM images. For a hexagonal lattice, $E_{\text{DM}}^{\text{Néel}} = -\sqrt{3}\pi d$,⁴⁸ where d is the

407 magnitude of the DMI vector. Therefore d in graphene/Co/Ru(0001) system can be estimated
408 as $d = 0.11 \pm 0.04$ meV per atom. Similarly, d in Co/Ru system can be estimated as
409 $d = -0.05 \pm 0.01$ meV per atom based on 3ML Co/Ru result (Fig. 3e) where roughly 45°
410 tilted magnetization with respect to the domain boundary (see two peaks at 135° and 225° in
411 Fig. 3e) indicates that the dipolar energy difference between Néel- and Bloch- DWs $E_d^{\text{Bloch}} -$
412 $E_d^{\text{Néel}}$ is comparable to the DMI energy $E_{\text{DM}}^{\text{Néel}}$. Here the error bar is given by the uncertainty
413 of the magnetization profile within in-plane region³⁶. Therefore, d at graphene/Co interface
414 with Co thickness ranged from 4-6 ML can be estimated as 0.16 ± 0.05 meV per atom,
415 based on the estimated d values in graphene/Co/Ru(0001) and in Co/Ru(0001).
416 **Data availability.** The data that support the findings of this study are available from the
417 corresponding authors upon reasonable request.

⁵⁶ Kresse, G. & Hafner, J. Ab initio molecular dynamics for liquid metals. *Phys. Rev. B* **47**, 558–561 (1993).

⁵⁷ Kresse, G. & Furthmüller, J. Efficient iterative schemes for ab initio total-energy calculations using a plane-wave basis set. *Phys. Rev. B* **54**, 11169–11186 (1996).

⁵⁸ Xiang, H. J., Kan, E. J., Wei, Su-Huai, Whangbo, M.-H. & Gong, X. G. Predicting the spin-lattice order of frustrated systems from first principles. *Phys. Rev. B* **84**, 224429 (2011).

⁵⁹ Bihlmayer, G., Kroteev, Y. M., Echenique, P. M., Chulkov, E. V. & Blugel, S. The Rashba-effect at metallic surfaces. *Surface Science* **600**, 3888 (2006).

⁶⁰ Sutter, P. W., Flege, J.-I. & Sutter, E. A. Epitaxial graphene on ruthenium. *Nature Mater.* **7**, 406–411 (2008).

⁶¹ Huang, L. et al., Intercalation of metal islands and films at the interface of epitaxially grown graphene and Ru(0001) surfaces. *Appl. Phys. Lett.* **99**, 163107 (2011).

⁶² El Gabaly, F. et al. Structure and morphology of ultrathin Co/Ru(0001) films. *New J. Phys.* **9**, 80 (2007)

⁶³ Liao et al. Intercalation of cobalt underneath a monolayer of graphene on Ru(0001). *Surf. Rev. Lett.* **19**, 1250041 (2012).

⁶⁴ Hubert, A. & Schäfer, R. *Magnetic Domains* (Springer, Berlin, 1998).

⁶⁵ Chen, G. et al. Out-of-plane chiral domain wall spin-structures in ultrathin in-plane magnets. *Nat. Commun.* **8**, 15302 (2017).

⁶⁶ Blundell, S. J. *Magnetism in Condensed Matter* (Oxford University Press, Oxford, 2001).